X-ray Mapping of Nanoparticle Superlattice Thin Films

Benjamin T. Diroll,[†] Vicky V. T. Doan-Nguyen,[‡] Matteo Cargnello,[†] E. Ashley Gaulding,[‡] Cherie R. Kagan,[†,‡,§] and Christopher B. Murray*[,†,‡]

[†]Department of Chemistry, [‡]Department of Materials Science and Engineering, and [§]Department of Electrical and Systems Engineering, University of Pennsylvania, Philadelphia, Pennsylvania 19104, United States

ABSTRACT We combine grazing-incidence and transmission small-angle X-ray diffraction with electron microscopy studies to characterize the structure of nanoparticle films with long-range order. Transmission diffraction is used to collect in-plane diffraction data from single grains and locally aligned nanoparticle superlattice films. Systematic mapping of samples can be achieved by translating the sample in front of the X-ray beam with a spot size selected to be on the order of superlattice grain features. This allows a statistical determination of superlattice grain size and size distribution over much larger areas than typically accessible with electron microscopy. Transmission X-ray measurements enables spatial mapping of the grain size, orientation, uniformity, strain, or crystal projections and polymorphs. We expand this methodology to binary nanoparticle superlattice and nanorod superlattice films. This study provides a framework for characterization of nanoparticle superlattices over large areas which complements or expands microstructure information from real-space imaging.

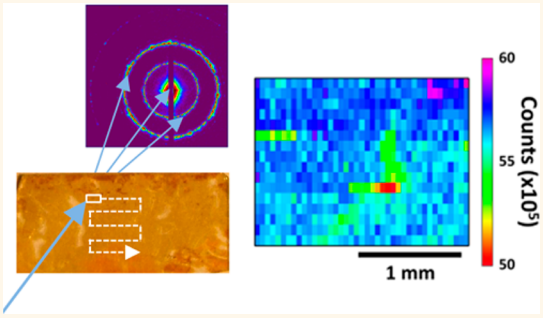

KEYWORDS: SAXS · GISAXS · nanoparticle superlattice · grain size · mapping

Monodisperse colloidal nanoparticles (NPs) self-assemble into nanoparticle superlattices (NSLs) with long-range translational symmetry analogous to atomic crystals or molecular liquid crystals.[1−3] Such NP assemblies demonstrate collective or emergent properties derived from the interaction of NSL building blocks at the nanometer length scale.[4,5] To realize these unique properties at any consequential scale requires the formation of NSLs over large areas. Recent work has demonstrated that NP assemblies grown on hydrophilic subphases can form large area (up to 1 cm^2) polycrystalline NSL thin-films that can be laminated on to arbitrary substrates and used as the active layer in electronic devices.[2] Moving to large scales requires new measurement techniques, as real-space imaging of NP assemblies by electron microscopy techniques is not feasible over such large areas. At the same time, device applications necessitate relevant figures of merit. Metrics of NSL quality—beyond showing NSL existence—are not standardized in the literature and are primarily limited to microscopic estimations of grain size, polymorphism, or defects.[6−10] Image analysis with autocorrelation provides a systematic method for defect analysis or to determine coherence length, but remains intrinsically local.[11] Applied across a large area, X-ray scattering techniques can avoid selection and exclusion biases that limit microscopy and provide information with greater statistical confidence.

Early reports of single-component NSLs and binary nanoparticle superlattices (BNSLs) were characterized primarily by electron microscopy, but subsequent work has employed transmission and grazing incidence small-angle X-ray scattering (TSAXS and GISAXS, respectively) to observe the structure and dynamics of NP assemblies. SAXS techniques have now been used extensively in crystal structure characterization and dynamical processes like evaporative self-assembly and solvent or thermal annealing by both *in situ* and *ex situ* methods.[12−23] Diffraction techniques have not, however, been used to study the two dimensional microstructure of colloidal NSLs in a systematic manner. Here we show that a combination of TSAXS and GISAXS on assembled NSL films

* Address correspondence to cbmurray@sas.upenn.edu.

Received for review November 3, 2014 and accepted December 5, 2014.

Published online December 05, 2014
10.1021/nn5062832

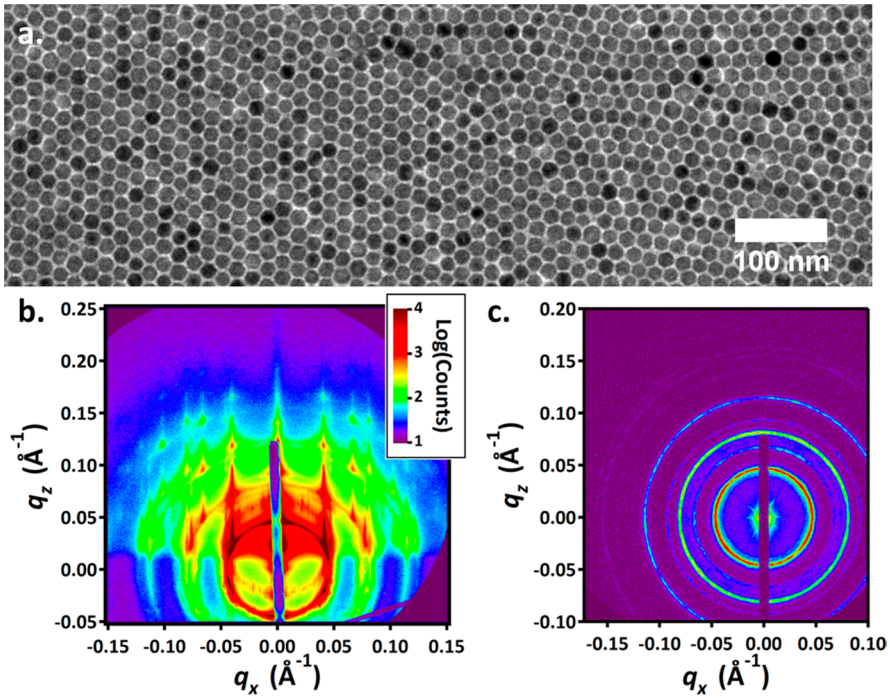

Figure 1. (a) TEM micrograph of Fe_3O_4 NPs self-assembled into a thin-film on diethylene glycol. (b) GISAXS and (c) TSAXS from a multilayer assembled film of the same NPs.

can be corroborated with electron microscopy to determine the structure of oriented NP films over large surface areas. Using a microfocused X-ray beam in transmission, we can resolve the X-ray diffraction patterns arising from single grains of single-component and binary NP assemblies. TSAXS data taken at hundreds of points across a sample can be used to map the orientation of NSL films in-plane, estimate the grain size and distribution, and map the homogeneity, presence of polymorphs, or distinct projections over total areas >1 mm^2 with few intrinsic limitations to reaching larger areas or higher resolutions. Mapping can be readily extended to BNSLs and assemblies of anisotropic NPs.

RESULTS AND DISCUSSION

To prepare NSL thin films for analysis, monodisperse NP samples were first synthesized by standard methods and then cast from organic solvents on to glycol subphases for self-assembly. Because the films float on an immiscible subphase, NSLs can be laminated on to arbitrary substrates. For this study, NSL membranes were deposited on to 0.25 mm thick quartz coverglass windows which allow high X-ray transparency and low small-angle background intensity for transmission measurements. Figure 1a shows a monolayer film composed of faceted 14 nm Fe_3O_4 NPs packed into a hexagonal lattice structure. Size- and shape-mismatched particles generate site defects and ultimately limit the crystal grain size in films made with this sample. Figure 1 panels b and c show GISAXS and TSAXS measurements of multilayer (>10 layers) NSL structures self-assembled from the same sample which fits to a *hcp* structure with dimensions a = 15.5 nm and c = 25.3 nm. The data also suggests lower symmetry defects (evidenced from small intensity at q = 0.0405 Å^{-1}) with additional lines of roughly 10% of the intensity of the hexagonal (100) peak consistent with a subset of cubic grains (Supporting Information Figure S1). The polycrystalline nature of the film is apparent from the rings of intensity at fixed q values in both the GISAXS and TSAXS data. Bright spots in the GISAXS data show that crystal growth from the glycol surface proceeds with a preferred orientation of the hexagonal c-axis growing vertically from the substrate. Rings of relatively homogeneous intensity in the transmission measurements indicate that the samples have an approximately random orientation of grains in the thin-film plane. Despite the limited grain size, Scherrer analysis, which has been used for other assemblies,[24] is not clearly applicable because instrumental line broadening constrains straightforward grain-size analysis under the experimental conditions to grains length dimensions of ~600 nm. For grains in which the intrinsic peak breadth is substantially sharper than the instrumental line-broadening (e.g., high-quality NSLs), Scherrer analysis is of tenuous value even after deconvolution of the instrumental contribution to broadening because the estimated broadening is then a strong function of the deconvolution.

NSLs of substantially larger grain size can be obtained with more monodisperse particles (<5% dispersions). Differences in grain size which may be difficult or tedious to ascertain from microscopic measurements can be easily resolved using a microfocused

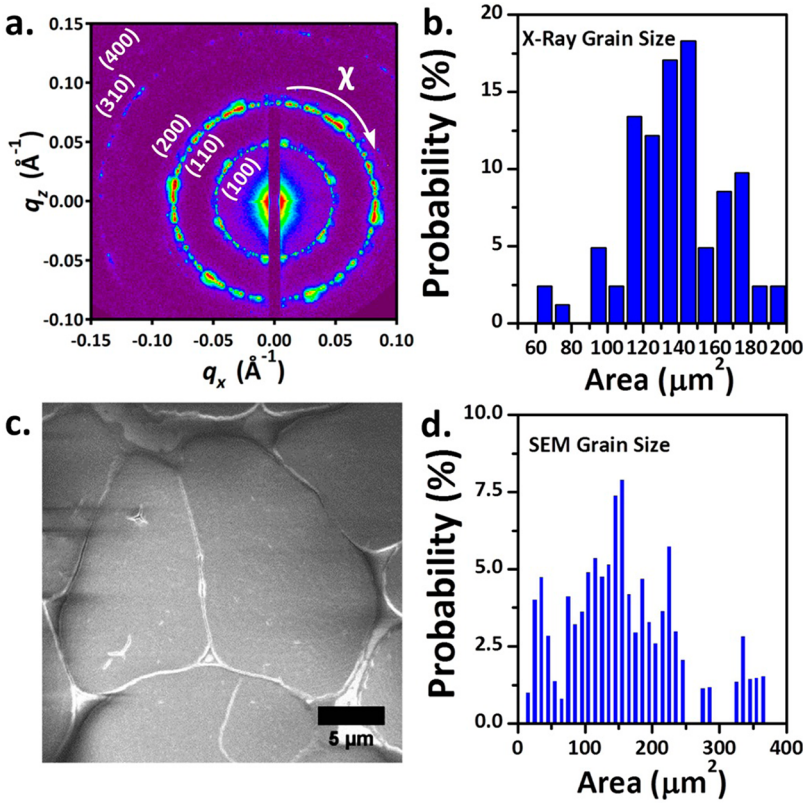

Figure 2. (a) Typical TSAXS data from an iron oxide NSL showing 6-fold symmetry and multiple diffraction rings. χ is labeled in the plot. (b) Area-weighted probability distribution of grain sizes estimated from X-ray diffraction measurements of the number of spots occurring within a single sampled spot. (c) SEM micrograph showing NSL grains. (d) Area-weighted probability distribution of grain sizes estimated from manual sizing of grains in SEM images.

X-ray source in transmission geometry. Figure 2a shows transmission data for a second sample of 13.5 nm Fe_3O_4 NPs self-assembled on diethylene glycol. This sample self-assembles into a six-eight layer film with *hcp* structure (a = 15.2 nm; c = 24.8) with the c-axis oriented perpendicular to the plane (see GISAXS data in Supporting Information Figure S2). The transmission SAXS data shows reflections from the allowed (100), (110), (200), (310), and (400) planes. The much larger grain size of this sample is apparent from the diffraction spots arising from single superlattice grains.[25,26] Further evidence that these spots arise from single crystals is that the spots appear with the appropriate multiplicity about χ (the angle around the ring). The peaks from the (100) and (110) planes exhibiting 6-fold symmetry are offset by the expected 30°, as seen in Figure 2a.

Data from this sample was collected at hundreds of locations. (Supporting Information Figure S3 contains additional TSAXS data.) By counting the number of single-crystal peaks apparent in the diffraction patterns of individual spots, which represent a defined beam area of 5000 μm^2 (50 μm $\times$ 100 μm), we can estimate the average grain area within a spot in a straightforward manner as area/number. Grain size is among the most important figures-of-merit for NSLs and this methodology offers a straightforward estimate of grain size, particularly well-suited for large grains that are not easily estimated using Scherrer techniques or microscopy. In this circumstance, the sample was chosen because both diffraction and microscopy measurements of grain size are possible. Diffraction sizing should be considered complementary to other techniques: very small grains (<500 nm) can be analyzed using the Scherrer methods or easily surveyed to obtain statistical distributions by SEM or TEM. This approach may undercount grains of very small size, if they do not diffract appreciably above the baseline, and it overcounts grains that appear in multiple spots, but neither of these extrema is problematic for this sample. Any voids or amorphous material will lead to overestimation of grain size with this technique. Ordinarily in a powder only a small fraction of grains within the sampled volume would satisfy the Bragg condition at a given reflection. But this method exploits the strong orientation of the film (c-axis growth transverse to the substrate plane with no (00c) peaks observed in TSAXS), which is commonly found in NSLs and BNSLs,[14,27,28] to assume that every grain within the sampling area satisfies the Bragg condition to generate diffraction spots on the detector at the (110) ring. Figure 2b shows a plot of the estimated grain area (5000 μm^2/number) using X-ray grain counting.

Grain size and grain size distributions have potential to provide insight into the mechanism of nucleation

and growth of NSLs. Under a model of nucleation and growth in which the two-dimensional film forms from random nuclei at random locations which then grow isotropically to form grain boundaries with other NSLs, the grains would appear as Voronoi tiles and should approximate a gamma distribution of areas.[29] The data in Figure 2b are consistent with this mechanism, but very likely could also fit other distributions of grain sizes. Figure 2c is an SEM image of the same film, showing the granular structure ascertained from X-ray measurements. Higher-resolution images confirm that the large structures apparent in Figure 2c are single superlattice grains (Supporting Information Figure S4). SEM only partially supports the film formation mechanism described above: grains show mostly straight boundaries with neighbors, but they also have rounded intersections rather than vertices. Curved grain edges are consistent with the Monte Carlo simulations of Rabini *et al.*,[30] who demonstrated similar two-dimensional domain edges tending toward disk shapes, as opposed to three-dimensional NSLs which adopt polyhedral geometries.[28]

By surveying 250 grains using SEM micrographs (see Supporting Information Figure S5 for more micrographs), we also generate an independent estimate of the grain size. Our analysis largely confirms the legitimacy of the approximations made in analyzing X-ray diffraction data: no grains were found smaller than 3 μm^2 (>20 000 unit cells) and amorphous material and voids were confined to small regions around grain boundaries. Figure 2d shows the area-weighted probability of grain sizes measured using low-magnification SEM images like that in Figure 2c, analogous to the X-ray grain size estimation. (The number distribution of grain areas is presented in Supporting Information Figure S6.) The grain area distribution measured by electron microscopy is broader than the distribution estimated by X-ray measurements, but the most probable grain area in both methods is ~150 μm^2. The broader dispersion of grain sizes estimated from SEM most likely arises from the smaller sampling spot size (1200 μm^2), which is limited by the detector size and working distance. The larger sampling area of the X-ray measurement is more likely to capture a statistical cross-section of the sample at any given spot.

Mapping samples with a microfocused X-ray beam allows determination of not only grain size and dispersion but also film uniformity, strain, orientation, crystal polymorphs or impurity phases, and defects or vacancies.[31,32] Crystal orientation is a critical parameter for microelectronics and bit-patterned media. Control over in-plane crystal orientation of NSLs remains primitive at present, but distinguishable properties along different zone axes of NSLs is likely, particularly for anisotropic NPs.[33−35] Although most studies of charge transport have focused on NP solids lacking long-range order, transport studies of polycrystalline[4,36] and single crystalline (or aligned) NSLs are possible.[37] TSAXS is an excellent way to map the orientation of crystal grains in-plane. Extending the detection range to include wide angles allows a determination of the orientation of crystal axes within the NPs forming a NSL.[26] In addition to specifying the crystal orientation within a beam spot and correlating that with its position on a sample, TSAXS also provides information about the film uniformity from total scattering and the spatial variation of polymorphs, projections, or impurity phases in the film.

Figure 3a is a cartoon of the mapping experiment used to analyze NSL films. To generate maps of the film surface, the sample position is incrementally shifted in an array pattern. Figure 3b shows a typical transmission SAXS pattern from a sample of 10 nm $CoFe_2O_4$ NPs crystallized into an *hcp* structure with unit cell a = 11.6 nm and b = 18.9 nm. Unlike the sample in Figure 2a, the intensity variation about χ is smooth. The structure within the beam spot is substantially oriented but individual NSLs are not resolved. Orientation may arise by several means, but in this instance the films are not globally oriented, yet have sufficiently large domains to achieve alignment across several samplings spots. Low resolution SEM evidence in Figure 3c shows fracturing patterns in a large grain structure which are distinct from the grain boundaries in Figure 2c. We hypothesize that gradual, small distortions in the grain orientation occur in the final drying step of the NSL, as has been speculated for aligned nanorod (NR) superlattices,[38] or from fracture processes during annealing acting akin to low-angle grain boundaries. The smooth variation in intensity versus χ shown in Figure 3b is interpretable as an in-plane small-angle pole figure showing the probability of orientations within the sample spot. The centered pole figure in Figure 3d shows that 59% of the sample is oriented within $\pm 5°$ of the peak orientation and an expanded window of $\pm 10°$ encompasses 85% of the intensity. Figure 3e is a map of the peak angle of the pole figure across the film, colored according to the maximum angle. The map demonstrates only very subtle changes in orientation over distances larger than 500 μm suggesting the potential of NPs to provide a tool for pattern multiplication through controlled placement[39] or directed self-assembly similar to block copolymers.[40,41]

Figure 4 shows maps generated from several hundred points of a 13.5 nm Fe_3O_4 NP film. Figure 4a tracks the intensity of a single point ($\Delta\chi < 1°$) of the (110) ring across the film. The data are colored according to the intensity of the point and although the global distribution of peak values at the arbitrary point appears random, local clustering of intensity is observed from large crystal grains that span adjoining sample spots or families of grains that have lost registry due to annealing or the final drying step. Figure 4b shows the integrated intensity of the (110) ring and provides a measure of film uniformity as the intensity depends

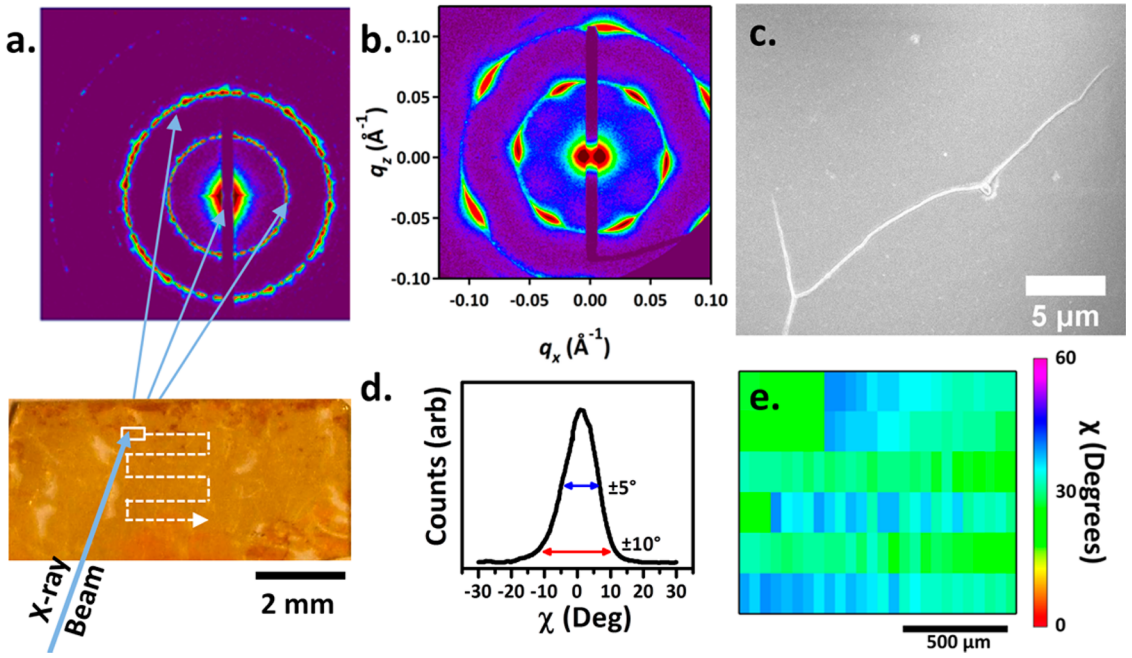

Figure 3. (a) Cartoon of raster pattern used to analyze samples superimposed over a photograph of one such sample; (b) TSAXS pattern of $CoFe_2O_4$ NP film; (c) low-magnification SEM image of 10 nm $CoFe_2O_4$ NP film; (d) in-plane small-angle pole figure of (100) reflection of $CoFe_2O_4$ NSL film; (e) color map of the angular maximum of the pole-figure for each sample spot.

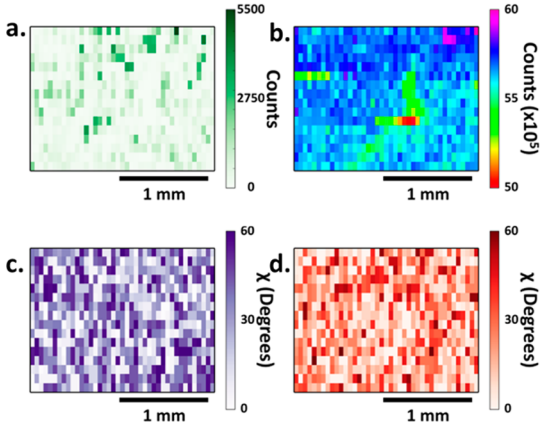

Figure 4. (a) Heatmap of the intensity of a single pixel along the (110) ring of an *hcp* NSL of 13.5 nm Fe_3O_4 NPs mapped at several hundred locations. (b) Heatmap of the same sample showing variation of the integrated intensity of the complete (110) ring. Panels c and d show the in-plane angular distribution of the most intense peak of the (100) and (110) reflections of the same sample within a given 60° window in χ.

primarily on the amount of material within the sampling volume which satisfies the Bragg condition. Data can be corrected for changes of beam intensity (see Supporting Information Figure S7) and fluctuations of the substrate scattering are small. The vast majority of the sample spots measured fall within a window of about 2%, indicating high uniformity of film thickness and crystallinity over ~4 mm^2. Furthermore, because the integration is performed at the same ring (fixed q), the high uniformity of intensity also implies uniform out-of-plane orientation and the absence of substantial impurities of different crystal structure. The largest difference in the integrated intensity between any of the spots is 14%, but in this instance it is speculated based upon the clustering of lower-intensity points that the reduced scattering comes from points spanning a scratch or crack made after NSL assembly, as are visible in a photograph of the sample (see Supporting Information Figure S8). Figure 4 panels c and d are orientation maps of the maximum intensity about the ring within a 60° window for the (100) and (110) reflections, respectively, of the *hcp* NSL thin film, colored to reflect the orientation angles. Close inspection again shows local clustering of most probable angles from large grains or grain families that dominate the signal. As expected based on the crystal structure, the peak intensities of the (100) and (110) rings are generally offset by 30°, confirming the same crystal structure across the sample.

Figure 5 demonstrates the application of TSAXS mapping applied to other NP assemblies. Figure 5 panels a, b, and c show TEM, GISAXS, and TSAXS of a four-layer simple hexagonal AlB_2-type BNSL assembled from 18 nm bismuth NPs and 6 nm gold NPs similar to previous reports.[27] Figure 5d shows a map of the in-plane orientation of the (100) reflection of the AlB_2 BNSL. Because the grain size is smaller and the beam spot size larger (~10000 μm^2), local clustering effects are less clear than in single-component NSLs. This sample demonstrates a limitation of the technique described above: the sample heterogeneity and the beamspot must be scaled to a similar order to extract information using these relatively simple analyses.

The influence of orientation on the optoelectronic properties of NRs and their assemblies is particularly

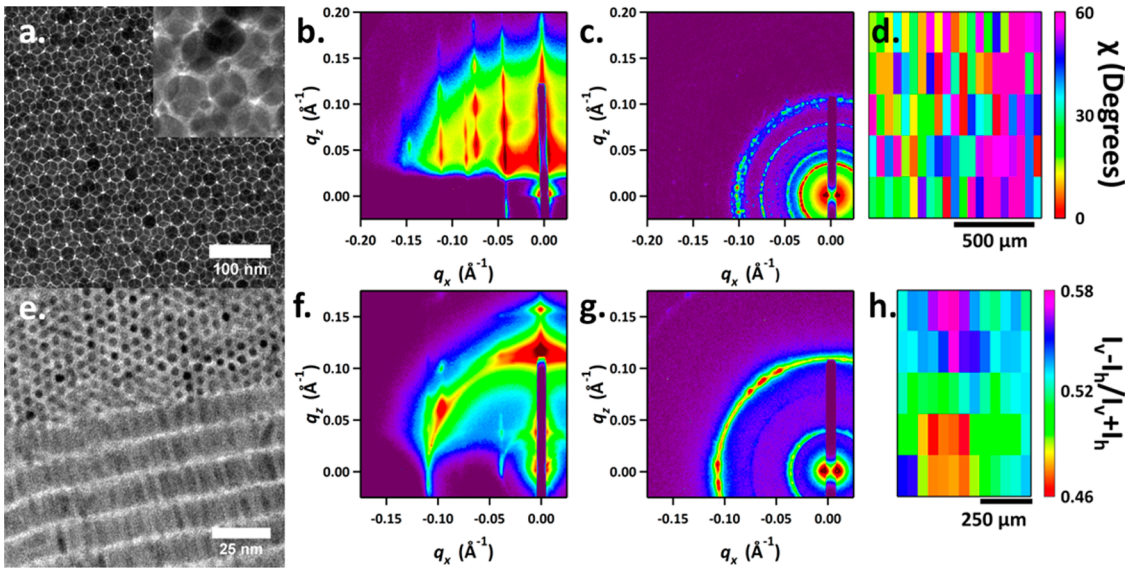

Figure 5. (a) TEM micrograph with higher magnification inset, (b) GISAXS, and (c) TSAXS of an AB_2 BNSL composed of Bi and Au NPs. (d) An orientation map of the maximum along the (100) ring from TSAXS patterns. (e) TEM, (f) GISAXS, and (g) TSAXS of a CdSe/CdS dot-in-rod NSL film. (h) An orientation map comparing the ratio of intensities of the lamellar (h, inner) spacing ring with the near-neighbor (v, outer) close-packed ring.

pronounced due to shape-induced polarization of the electronic structure.[33,34,37] Figure 5 panels e, f, and g show TEM, GISAXS, and TSAXS of a NR superlattice film composed of 4.1 nm × 16 nm CdSe/CdS dot-in-rod heterostructures. Self-assembly of NRs at liquid interfaces yields two distinct morphologies: multilayer lamellae with NRs lying with their long axes in-plane and monolayers hexagonally packed NRs standing vertically with respect to the surface.[13] Depending on whether NRs with long-axes in-plane assemble hexagonally within lamellae, these morphologies can be understood as two projections of smectic B ordering or smectic A/B polymorphs. Figure 5e demonstrates that both of these structures persist when removed from the liquid subphase, and Supporting Information Figure S9 shows that they can even coexist on top of one another. Figure 5g shows two prominent rings with spots from large NSLs corresponding to the two morphologies in Figure 5e. Diffraction is generally a poor technique for absolute purity analysis (particularly for amorphous impurities), but relative estimates of sample polymorphism can be made for samples with modest (>5%) fractions of crystalline impurities. Here, TSAXS measurements are used to describe the spatial variation of the two NR morphologies by observing the ratio of intensity between the reflection at 0.036 Å^{-1} arising from the lamellar spacing with the intensity of the reflection at 0.107 Å^{-1} arising primarily from the vertically-aligned hexagonal packing of NRs (evidenced from 6-fold symmetry). Figure 5h maps the film structure polarization, defined as $(I_{vertical} - I_{horizontal})/(I_{vertical} + I_{horizontal})$, demonstrating that the heterogeneity of polymorphism occurs over a scale >500 μm in length.

CONCLUSIONS

A combination of GISAXS, TSAXS, and electron microscopy has been used to characterize the film structure of large-scale NSLs. TSAXS measurements of thin films allow an estimation of the NSL grain size and size distribution based on X-ray measurements which compare reasonably with the tedious method of direct microscopic measurements of grain size. By translating the sample in front of the beam, systematic mapping of NSL films can be used to map sample properties including grain size, grain orientations, polymorphs, and homogeneity. Although performed on a synchrotron beamline, laboratory SAXS instrumentation is capable of many similar analyses if the scale of the NSL grain size is matched to the beam spot size, which is increasingly possible using microdiffraction or larger-grained samples. These techniques were applied to single-component, binary, and anisotropic NP assemblies to map film uniformity, orientation, and polymorphism.

METHODS

Synthesis and Assembly of NPs. Fe_3O_4 NPs,[42] $CoFe_2O_4$ NPs,[43] Bi NPs,[44] Au NPs,[45] and CdSe/CdS dot-in-rod NPs[46] used in this study were synthesized by previously published methods. Self-assembly was performed on glycol subphases as previously described[2] and the films were dried on to quartz coverglass substrates. Briefly, 15−30 μL of 5−5 mg/mL solutions of NCs in hexanes was cast on to a room temperature subphase of 1.7 mL of diethylene glycol in a 1.5 cm × 1.5 cm × 1 cm (depth) Teflon well, which was immediately covered by a glass microscope

slide. After 1 h, the film was dry and picked-up on to the desired substrate, then held under vacuum for at least 6 h to completely remove remaining diethylene glycol.

X-ray Characterization. TSAXS and GISAXS measurements were performed at the X9 Beamline at the National Synchrotron Light Source (Brookhaven National Laboratory). The beam spot size varied between 100 μm wide $\times$ 50 μm tall and 250 μm wide $\times$ 50 μm tall. The beam energy was 13.5 keV, the sample-to-detector distance was set to 3 m, and detection was performed using a Mar CCD detector. Typical sampling times for GISAXS measurements were 3−10 s and typical sampling times for transmission measurements were 6−30 s. These conditions appeared to have no negative effects on the structures measured, which did not change over multiple measurements. Image processing was performed using GISAXS Shop and a in-house Python script.

Electron Microscopy. Transmission electron microscopy (TEM) was performed using a JEOL 1400 microscope operated at 120 keV. Scanning electron microscopy (SEM) was performed using a JEOL 7500 SEM operated at 5 keV. To prepare a sample for SEM imaging on quartz coverglass, the NP film was annealed in air at 400 °C for 30 min using a rapid thermal annealer (ULVAC), a procedure which was previously demonstrated to preserve NSL order and make conductive assemblies of ferrite NPs.[47,48] All studies of the samples were performed after annealing. Image processing was performed using ImageJ.

Conflict of Interest: The authors declare no competing financial interest.

Supporting Information Available: Additional microscopy and X-ray data. This material is available free of charge *via* the Internet at http://pubs.acs.org.

Acknowledgment. The authors thank K. Yager for many helpful discussions regarding experimental design and data analysis. Sample preparation and microscopy was supported by the Department of Energy, Office of Basic Energy Sciences, Division of Materials Science Award No. De-SC0002158. Work performed at the Center for Functional Nanomaterials and the National Synchrotron Light Source, Brookhaven National Laboratory was supported by the U.S. Department of Energy, Office of Basic Energy Sciences, under Contract No. DE-AC02-98CH10886. C.B.M. acknowledges the Richard Perry University Professorship.

REFERENCES AND NOTES

1. Shevchenko, E. V.; Talapin, D. V.; Kotov, N. A.; O'Brien, S.; Murray, C. B. Structural Diversity in Binary Nanoparticle Superlattices. *Nature* **2006**, *439*, 55–59.
2. Dong, A.; Chen, J.; Vora, P. M.; Kikkawa, J. M.; Murray, C. B. Binary Nanocrystal Superlattice Membranes Self-Assembled at the Liquid−Air Interface. *Nature* **2010**, *466*, 474–477.
3. Murray, C. B.; Kagan, C. R.; Bawendi, M. G. Self-Organization of CdSe Nanocrystallites into Three-Dimensional Quantum Dot Superlattices. *Science* **1995**, *270*, 1335–1338.
4. Urban, J. J.; Talapin, D. V.; Shevchenko, E. V.; Kagan, C. R.; Murray, C. B. Synergism in Binary Nanocrystal Superlattices Leads to Enhanced p-Type Conductivity in Self-Assembled PbTe/Ag_2 Te Thin Films. *Nat. Mater.* **2007**, *6*, 115–121.
5. Chen, J.; Dong, A.; Cai, J.; Ye, X.; Kang, Y.; Kikkawa, J. M.; Murray, C. B. Collective Dipolar Interactions in Self-Assembled Magnetic Binary Nanocrystal Superlattice Membranes. *Nano Lett.* **2010**, *10*, 5103–5108.
6. Evers, W. H.; De Nijs, B.; Filion, L.; Castillo, S.; Dijkstra, M.; Vanmaekelbergh, D. Entropy-Driven Formation of Binary Semiconductor-Nanocrystal Superlattices. *Nano Lett.* **2010**, *10*, 4235–4241.
7. Rupich, S. M.; Shevchenko, E. V.; Bodnarchuk, M. I.; Lee, B.; Talapin, D. V. Size-Dependent Multiple Twinning in Nanocrystal Superlattices. *J. Am. Chem. Soc.* **2010**, *132*, 289–296.
8. Bodnarchuk, M. I.; Kovalenko, M. V.; Heiss, W.; Talapin, D. V. Energetic and Entropic Contributions to Self-Assembly of Binary Nanocrystal Superlattices: Temperature as the Structure-Directing Factor. *J. Am. Chem. Soc.* **2010**, *132*, 11967–11977.
9. Bodnarchuk, M. I.; Shevchenko, E. V.; Talapin, D. V. Structural Defects in Periodic and Quasicrystalline Binary Nanocrystal Superlattices. *J. Am. Chem. Soc.* **2011**, *133*, 20837–20849.
10. Friedrich, H.; Gommes, C. J.; Overgaag, K.; Meeldijk, J. D.; Evers, W. H.; de Nijs, B.; Boneschanscher, M. P.; de Jongh, P. E.; Verkleij, A. J.; de Jong, K. P.; *et al.* Quantitative Structural Analysis of Binary Nanocrystal Superlattices by Electron Tomography. *Nano Lett.* **2009**, *9*, 2719–2724.
11. Pichler, S.; Bodnarchuk, M. I.; Kovalenko, M. V.; Yarema, M.; Springholz, G.; Talapin, D. V.; Heiss, W. Evaluation of Ordering in Single-Component and Binary Nanocrystal Superlattices by Analysis of their Autocorrelation Functions. *ACS Nano* **2011**, *5*, 1703–1712.
12. Lu, C.; Akey, A. J.; Dahlman, C. J.; Zhang, D.; Herman, I. P. Resolving the Growth of 3D Colloidal Nanoparticle Superlattices by Real-Time Small-Angle X-ray Scattering. *J. Am. Chem. Soc.* **2012**, *134*, 18732–18738.
13. Pietra, F.; Rabouw, F. T.; Evers, W. H.; Byelov, D. V.; Petukhov, A. V.; de Mello Donegá, C.; Vanmaekelbergh, D. Semiconductor Nanorod Self-Assembly at the Liquid/Air Interface Studied by *in Situ* GISAXS and *ex Situ* TEM. *Nano Lett.* **2012**, *12*, 5515–5523.
14. Hanrath, T.; Choi, J. J.; Smilgies, D.-M. Structure/processing Relationships of Highly Ordered Lead Salt Nanocrystal Superlattices. *ACS Nano* **2009**, *3*, 2975–2988.
15. Yu, Y.; Bosoy, C. A.; Smilgies, D.-M.; Korgel, B. A. Self-Assembly and Thermal Stability of Binary Superlattices of Gold and Silicon Nanocrystals. *J. Phys. Chem. Lett.* **2013**, *4*, 3677–3682.
16. Goodfellow, B. W.; Rasch, M. R.; Hessel, C. M.; Patel, R. N.; Smilgies, D.-M.; Korgel, B. A. Ordered Structure Rearrangements in Heated Gold Nanocrystal Superlattices. *Nano Lett.* **2013**, *13*, 5710–5714.
17. Korgel, B. A.; Fitzmaurice, D. Small-Angle X-ray-Scattering Study of Silver-Nanocrystal Disorder-Order Phase Transitions. *Phys. Rev. B* **1999**, *59*, 191–201.
18. Korgel, B.; Fitzmaurice, D. Condensation of Ordered Nanocrystal Thin Films. *Phys. Rev. Lett.* **1998**, *80*, 3531–3534.
19. Auyeung, E.; Li, T. I. N. G.; Senesi, A. J.; Schmucker, A. L.; Pals, B. C.; de la Cruz, M. O.; Mirkin, C. A. DNA-Mediated Nanoparticle Crystallization into Wulff Polyhedra. *Nature* **2014**, *505*, 73–77.
20. Connolly, S.; Fullam, S.; Korgel, B.; Fitzmaurice, D. Time-Resolved Small-Angle X-ray Scattering Studies of Nanocrystal Superlattice Self-Assembly. *J. Am. Chem. Soc.* **1998**, *120*, 2969–2970.
21. Narayanan, S.; Wang, J.; Lin, X.-M. Dynamical Self-Assembly of Nanocrystal Superlattices during Colloidal Droplet Evaporation by in situ Small Angle X-Ray Scattering. *Phys. Rev. Lett.* **2004**, *93*, 135503.
22. Korgel, B. A.; Zaccheroni, N.; Fitzmaurice, D. Melting Transition of a Quantum Dot Solid: Collective Interactions Influence the Thermally-Induced Order−Disorder Transition of a Silver Nanocrystal Superlattice. *J. Am. Chem. Soc.* **1999**, *121*, 3533–3534.
23. Altamura, D.; Holý, V.; Siliqi, D.; Lekshmi, I. C.; Nobile, C.; Maruccio, G.; Cozzoli, P. D.; Fan, L.; Gozzo, F.; Giannini, C. Exploiting GISAXS for the Study of a 3D Ordered Superlattice of Self-Assembled Colloidal Iron Oxide Nanocrystals. *Cryst. Growth Des.* **2012**, *12*, 5505–5512.
24. Smilgies, D.-M. Scherrer Grain-Size Analysis Adapted to Grazing-Incidence Scattering with Area Detectors. *J. Appl. Crystallogr.* **2009**, *42*, 1030–1034.
25. Hirsch, P. B. The Determination of Grain Size from Spotty X-ray Diffraction Rings. *Br. J. Appl. Phys.* **1954**, *5*, 257–260.
26. Li, R.; Bian, K.; Hanrath, T.; Bassett, W. A.; Wang, Z. Decoding the Superlattice and Interface Structure of Truncate PbS Nanocrystal-Assembled Supercrystal and Associated Interaction Forces. *J. Am. Chem. Soc.* **2014**, *136*, 12047–12055.
27. Smith, D. K.; Goodfellow, B.; Smilgies, D.-M.; Korgel, B. A. Self-Assembled Simple Hexagonal AB(2) Binary

Nanocrystal Superlattices: SEM, GISAXS, and Defects. *J. Am. Chem. Soc.* **2009**, *131*, 3281–3290.
28. Murray, C. B.; Kagan, C. R.; Bawendi, M. G. Synthesis and Characterization of Monodisperse Nanocrystals and Close-Packed Nanocrystal Assemblies. *Annu. Rev. Mater. Sci.* **2000**, *30*, 545–610.
29. Tanemura, M. Statistical Distributions of Poisson Voronoi Cells in Two and Three Dimensions. *Forma* **2003**, *18*, 221–247.
30. Rabani, E.; Reichman, D. R.; Geissler, P. L.; Brus, L. E. Drying-Mediated Self-Assembly of Nanoparticles. *Nature* **2003**, *426*, 271–274.
31. Murray, C. E.; Ying, A. J.; Polvino, S. M.; Noyan, I. C.; Cai, Z. Nanoscale Strain Characterization in Microelectronic Materials Using X-ray Diffraction. *Powder Diffr.* **2012**, *25*, 108–113.
32. Robinson, I.; Harder, R. Coherent X-ray Diffraction Imaging of Strain at the Nanoscale. *Nat. Mater.* **2009**, *8*, 291–298.
33. Steiner, D.; Azulay, D.; Aharoni, A.; Salant, A.; Banin, U.; Millo, O. Photoconductivity in Aligned CdSe Nanorod Arrays. *Phys. Rev. B* **2009**, *80*, 195308.
34. Persano, A.; De Giorgi, M.; Fiore, A.; Cingolani, R.; Manna, L.; Cola, A.; Krahne, R. Photoconduction Properties in Aligned Assemblies of Colloidal CdSe/CdS Nanorods. *ACS Nano* **2010**, *4*, 1646–1652.
35. Overgaag, K.; Liljeroth, P.; Grandidier, B.; Vanmaekelbergh, D. Scanning Tunneling Spectroscopy of Individual PbSe Quantum Dots and Molecular Aggregates Stabilized in an Inert Nanocrystal Matrix. *ACS Nano* **2008**, *2*, 600–606.
36. Dong, A.; Jiao, Y.; Milliron, D. J. Electronically Coupled Nanocrystal Superlattice Films by in Situ Ligand Exchange at the Liquid−Air Interface. *ACS Nano* **2013**, *7*, 10978–10984.
37. Rivest, J. B.; Swisher, S. L.; Fong, L.-K.; Zheng, H.; Alivisatos, A. P. Assembled Monolayer Nanorod Heterojunctions. *ACS Nano* **2011**, *5*, 3811–3816.
38. Baker, J. L.; Widmer-Cooper, A.; Toney, M. F.; Geissler, P. L.; Alivisatos, A. P. Device-Scale Perpendicular Alignment of Colloidal Nanorods. *Nano Lett.* **2010**, *10*, 195–201.
39. Akey, A.; Lu, C.; Yang, L.; Herman, I. P. Formation of Thick, Large-Area Nanoparticle Superlattices in Lithographically Defined Geometries. *Nano Lett.* **2010**, *10*, 1517–1521.
40. Ruiz, R.; Kang, H.; Detcheverry, F. A.; Dobisz, E.; Kercher, D. S.; Albrecht, T. R.; de Pablo, J. J.; Nealey, P. F. Density Multiplication and Improved Lithography by Directed Block Copolymer Assembly. *Science* **2008**, *321*, 936–939.
41. Yang, J. K. W.; Jung, Y. S.; Chang, J.-B.; Mickiewicz, R. A.; Alexander-Katz, A.; Ross, C. A.; Berggren, K. K. Complex Self-Assembled Patterns Using Sparse Commensurate Templates with Locally Varying Motifs. *Nat. Nanotechnol.* **2010**, *5*, 256–260.
42. Park, J.; An, K.; Hwang, Y.; Park, J.-G.; Noh, H.-J.; Kim, J.-Y.; Park, J.-H.; Hwang, N.-M.; Hyeon, T. Ultra-Large-Scale Syntheses of Monodisperse Nanocrystals. *Nat. Mater.* **2004**, *3*, 891–895.
43. Hyeon, T.; Chung, Y.; Park, J.; Lee, S. S.; Kim, Y.-W.; Park, B. H. Synthesis of Highly Crystalline and Monodisperse Cobalt Ferrite Nanocrystals. *J. Phys. Chem. B* **2002**, *106*, 6831–6833.
44. Yarema, M.; Kovalenko, M. V.; Hesser, G.; Talapin, D. V.; Heiss, W. Highly Monodisperse Bismuth Nanoparticles and Their Three-Dimensional Superlattices. *J. Am. Chem. Soc.* **2010**, 2–3.
45. Peng, S.; Lee, Y.; Wang, C.; Yin, H.; Dai, S.; Sun, S. A Facile Synthesis of Monodisperse Au Nanoparticles and their Catalysis of CO Oxidation. *Nano Res.* **2008**, *1*, 229–234.
46. Carbone, L.; Nobile, C.; De Giorgi, M.; Sala, F. D.; Morello, G.; Pompa, P.; Hytch, M.; Snoeck, E.; Fiore, A.; Franchini, I. R.; *et al*. Synthesis and Micrometer-scale Assembly of Colloidal CdSe/CdS Nanorods Prepared by a Seeded Growth Approach. *Nano Lett.* **2007**, *7*, 2942–2950.
47. Dong, A.; Chen, J.; Ye, X.; Kikkawa, J. M.; Murray, C. B. Enhanced Thermal Stability and Magnetic Properties in NaCl-Type FePt-MnO Binary Nanocrystal Superlattices. *J. Am. Chem. Soc.* **2011**, *133*, 13296–9.
48. Chen, J.; Ye, X.; Oh, S. J.; Kikkawa, J. M.; Kagan, C. R.; Murray, C. B. Bistable Magnetoresistance Switching in Exchange-Coupled $CoFe_2O_4$-Fe_3O_4 Binary Nanocrystal Superlattices by Self-Assembly and Thermal Annealing. *ACS Nano* **2013**, *7*, 1478–1486.